Journal of Materials Chemistry A

ROYAL SOCIETY OF CHEMISTRY

PAPER

View Article Online
View Journal | View Issue

Cite this: J. Mater. Chem. A, 2026, 14, 15034

Impact of the polymer donor side-chain length on the formation and processing of waterborne nanoparticles for organic solar cells

Hugo Laval,†*[a] Martina Rimmele, †*[b] Alberto Peinador Veiga, [c] Xabier Rodríguez-Martínez, [c] Gilles Pécastaings, [e] Marc Schmutz, [f] Alejandro Salinas-Villasenor,[g] Christine Lartigau-Dagron, [g] Antoine Bousquet, [g] Guillaume Wantz, [a] Jaime Martin, [cd] Martin Heeney [bh] and Sylvain Chambon *[a]

Organic photovoltaics (OPVs) have recently exceeded 20% power conversion efficiency (PCE), reinforcing their potential for commercialisation. However, large-scale adoption also depends on environmental impact, toxicity, cost, stability, and scalability. Conventional wet-processing routes typically rely on hazardous organic solvents, whereas aqueous nanoparticle (NP) dispersions offer a greener alternative and have already enabled device efficiencies above 10%. Yet strategies to tailor conjugated materials specifically for NP-based processing remain unexplored. This work examines how the alkyl side-chain length influences the performance of nanoparticle bulk heterojunctions. We investigated three conjugated polymers, FO4-T, FO6-T, and FO8-T, which were derived from a benzo[*c*][1,2,5]thiadiazole-based backbone and bear 2-butyl-1-octoxy, 2-hexyl-1-decoxy and 2-octyl-1-dodecoxy side chains, respectively. Donor–acceptor blend NPs were prepared *via* the miniemulsion method using Y6 as the non-fullerene acceptor. We correlated optical properties, NP characteristics, film microstructures, thermal annealing behaviour, and device performances to the macromolecular structure. Our findings show that the side-chain length strongly influences nanoparticle-based thin film morphology, its behaviour upon thermal treatment and the resulting photovoltaic efficiency. Among the series, FO8-T : Y6 exhibited the most favourable microstructure with a thermal treatment lower than its FO4-T and FO6-T counterparts and delivered power conversion efficiencies up to 10.64%. This study establishes structure–property relationships for water-processed organic solar cells and highlights side-chain engineering as a key lever for advancing eco-friendly, high-performance active layers.

Received 5th January 2026
Accepted 1st March 2026

DOI: 10.1039/d6ta00092d

rsc.li/materials-a

1 Introduction

Over the past year, the organic photovoltaic (OPV) community has finally surpassed the 20% power conversion efficiency (PCE) milestone, with reported certified efficiencies up to 20.8%.[1–3] This advancement underscores OPV's promise for expanding the photovoltaic market, yet high PCE alone is insufficient for commercialization. Other factors such as upscaling of organic solar cells (OSCs), their toxicity, stability, overall cost and life cycle need to be taken into consideration and addressed for their commercial success.[4–8] The lab-to-fab transition is enabled by using wet-process fabrication techniques that present the advantage of being low-cost and versatile to produce large-area OSCs.[9] However, they often require hazardous organic solvents, such as halogenated or chlorinated compounds, which pose significant safety and environmental concerns. Numerous studies have explored the use of green (or greener) solvents for the deposition of photoactive materials, but few have evaluated all the factors necessary for solvent sustainability, including environmental impact, hazard potential and feedstock origin.[10–13] Several solvent selection guides have been developed as tools to assess the sustainability of a solvent for its use in industry.[14] However, only a few solvents qualify as genuinely "green", and even fewer form efficient active layers for OSCs. While water is often considered an ideal sustainable solvent, its

[a]*Université de Bordeaux, CNRS, Bordeaux INP, IMS, UMR 5218, F-33400 Talence, France. E-mail: hlaval-iis@g.ecc.u-tokyo.ac.jp; sylvain.chambon@u-bordeaux.fr*

[b]*Department of Chemistry and Centre for Processable Electronics, Imperial College London, London W12 0BZ, UK. E-mail: martina.rimmele@imperial.ac.uk*

[c]*Universidade da Coruña, Campus Industrial de Ferrol, CITENI, Campus de Esteiro S/N, 15471 Ferrol, Spain*

[d]*Oportunius Programme, Axencia Galega de Innovacion, Xunta de Galicia, Galicia, Spain*

[e]*Univ. Bordeaux, CNRS, CRPP, UMR 5031, F-33600 Pessac, France*

[f]*Université de Strasbourg, CNRS, Institut Charles Sadron, PLAMICS, F67000 Strasbourg, France*

[g]*Universite de Pau et Pays de l'Adour, CNRS, IPREM, Pau, France*

[h]*King Abdullah University of Science and Technology (KAUST), Thuwal, 23955-6900, Saudi Arabia*

† Authors contributed equally.

practical relevance for OPVs is limited by the poor solubility of most organic semiconductors. Efforts to solubilize these materials in water or water/alcohol mixtures for photoactive layer deposition have typically resulted in low efficiencies, as they often rely on incorporating bulky, water-compatible side groups which are detrimental to electrical properties. This challenge can be overcome by the fabrication of aqueous dispersions of organic semiconductor nanoparticles. Since the introduction of the miniemulsion method by Landfester *et al.* in the early 2000s, this strategy has evolved and now represents a viable route for producing eco-friendly OSCs with efficiencies exceeding 10%.[15–19]

In addition to providing a safer and cleaner route to form the active layer, this strategy allows researchers to harness the unique form factor of the nanoparticles to control the active layer morphology.[20] Nevertheless, more fundamental studies are needed to guide the development of high performing, water-processed active layers. Building on efforts to develop organic semiconductors compatible with green solvents, new design strategies need to be established for conjugated materials tailored to be processed as nanoparticles suitable for efficient OSCs.[21]

Alkyl side chains play a crucial role in conjugated polymers by enhancing their solubility and, in turn, their processability. Beyond this, side-chain modification can significantly influence the properties of both the polymers themselves and the OSCs derived from them.[22] For example, while longer side chains generally improve solubility, they can hinder charge transport and disrupt optimal phase segregation. Moreover, careful side-chain engineering has been shown to promote favorable molecular aggregation and improve crystallinity.[23–26]

In the preparation of bulk heterojunction nanoparticles (np-BHJ), parameters such as the synthesis method (miniemulsion or nanoprecipitation) and the choice of the surfactant can remarkably impact the internal nanoparticle morphology and processability of np-BHJ.[27] Evaluating whether variations in the polymer alkyl side chain length exert a comparable influence is essential for optimizing the np-BHJ formulation for high-efficiency OSCs. Previous studies have shown that changing from linear to branched alkyl side chains alters the internal morphology of the nanoparticles through changes in the surface energy.[28,29] However, a systematic investigation into the impact of the branching chain length on nanoparticle formation and OPV device performance is yet to be established.

In our previous work, we developed a versatile two-step synthetic approach to construct a library of conjugated polymers incorporating a benzo[*c*][1,2,5]thiadiazole electron–acceptor unit, which readily enabled the introduction of different alkoxy chains.[30] By further combining this unit with thiophene-based electron–donor units, a broad range of polymer structures were screened. Among these, the co-polymer with thiophene, FO6-T, proved particularly promising, achieving a power conversion efficiency (PCE) of 15.4% in a binary blend with L8-BO as the acceptor and good device stability.[31] In addition to its good OPV performance, its low synthetic complexity makes it an attractive candidate for potential upscaling. Herein, we focus on three different polymers, namely FO4-T, FO6-T and FO8-T, with different alkoxy side chains, 2-butyl-1-octoxy, 2-hexyl-1-decoxy and 2-octyl-1-dodecoxy, respectively (Fig. 1a). The number in the polymer name denotes the length of the shorter alkyl chain in the branched structure. The objective of this study is to investigate the influence of side-chain length on the performance of nanoparticle-based (NP) active-layer OPV devices, as well as on the thermal annealing temperature necessary to induce NP coalescence. For this purpose, the non-fullerene acceptor Y6 (ref. 32) was employed as the small-molecule acceptor, forming composite donor/acceptor nanoparticles with each FO*x*-T polymer *via* the miniemulsion method. The optical properties, physical characteristics and device performances of the polymers with Y6 were analyzed and correlated with the microstructures of the films. As a result, we present a comprehensive study on their structure–property relationships, as well as report a high performing NP-based OSC blend, FO8-T : Y6, obtaining device efficiencies of up to 10.64%.

2 Results and discussion

2.1 FO*x*-T : Y6 aqueous dispersion preparation and characterization

Following the miniemulsion protocol, colloidal dispersions were obtained by mixing an organic phase containing either FO4-T : Y6, FO6-T : Y6 or FO8-T : Y6 (see Fig. 1a) in a chloroform solution with a water phase consisting of the surfactant sodium dodecyl sulfate (SDS) in water. For all three dispersions, the donor : acceptor ratio was kept at 1 : 1.2 and their initial concentration in chloroform was 35 mg ml^{-1}. The ratio between the organic and aqueous phase was kept at 1 : 5 and the concentration of the surfactant in water was 5 mg ml^{-1}. Finally, stable colloidal dispersions were obtained with a similar diameter for all three dispersions, around 60 nm, measured by means of dynamic light scattering (DLS) (Fig. S2 and Table S2). To investigate the internal nanoparticle morphology and verify their size, cryogenic transmission electron microscopy (cryo-TEM) measurements were conducted (Fig. 1b and S3), confirming particle sizes of approximately 60 nm in all cases. Moreover, the images reveal that the nanoparticles were predominantly spherical, but morphology and size distribution were somewhat dependent on side-chain length. FO8-T : Y6 showed the most uniform and well-defined particles, whereas FO6-T : Y6 exhibited greater polydispersity and partial aggregation.

UV-visible absorbance spectroscopy was performed for each of the three dispersions, as shown in Fig. 1c. All polymers exhibited similar spectral features, with an absorption peak in the high energy region around 350–400 nm, and two additional peaks in the lower energy region from 600 to 700 nm. Therefore, in these regions, the synthesized nanoparticles of FO*x*-T : Y6 share the same spectral signature. Looking more closely in the Y6 region (700–850 nm), the composite nanoparticle FO8-T : Y6 presents a higher contribution of Y6 absorption. This is probably due to a lower absorption coefficient of the FO8-T polymer as previously observed for polymers when increasing the side chain length.[33]

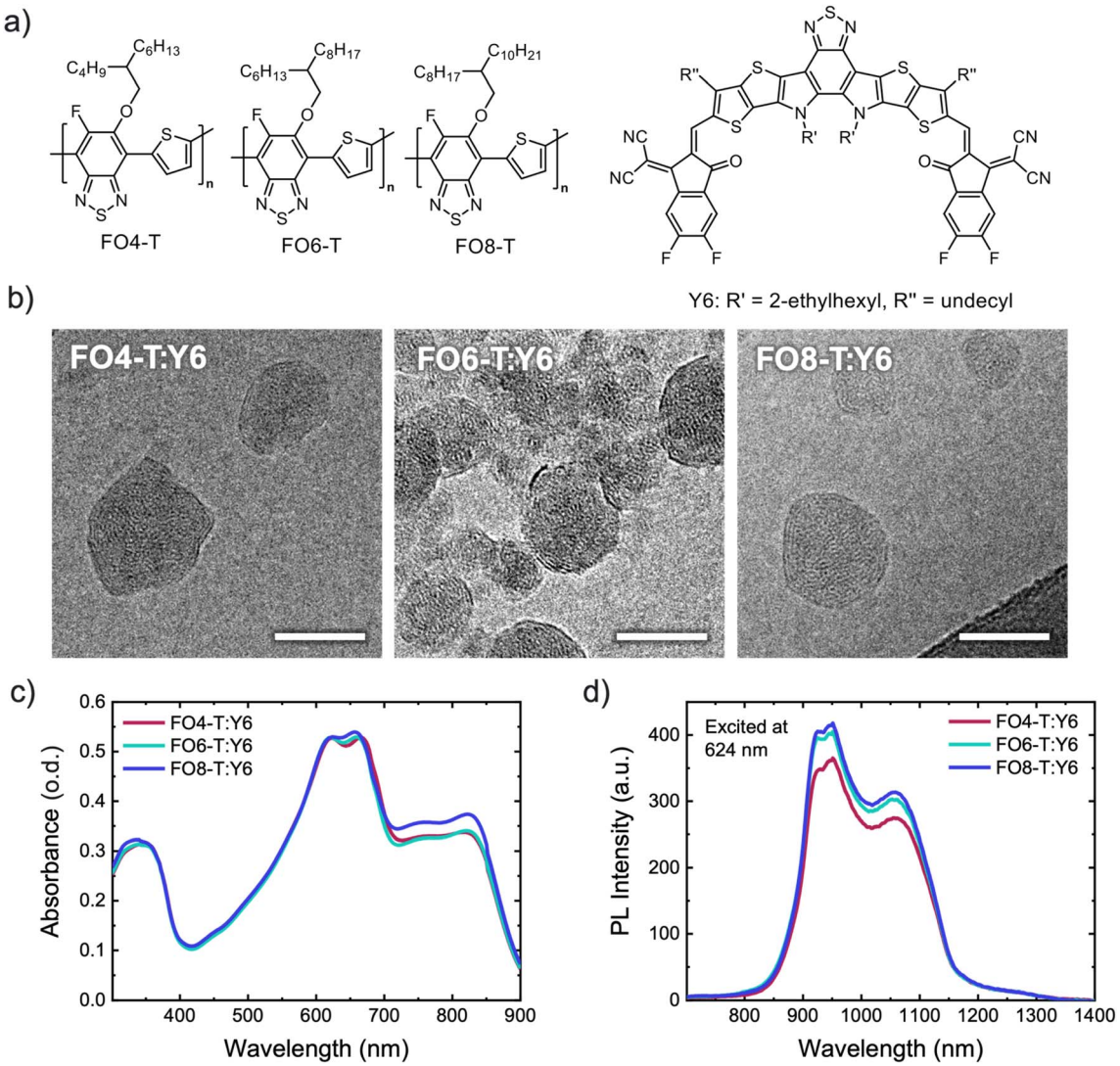

Fig. 1 (a) Chemical structures of FO4-T, FO6-T, and FO8-T donor polymers and the Y6 acceptor small molecule. (b) Cryo-TEM images of FO4-T : Y6, FO6-T : Y6 and FO8-T : Y6 composite nanoparticles (scale bars are 50 nm). (c) UV-visible absorption and (d) PL spectra of FO4-T : Y6, FO6-T : Y6, FO8-T : Y6 nanoparticle dispersions. The wavelength of the PL excitation was set at 624 nm.

Photoluminescence (PL) of the np-BHJ was measured in dispersion to investigate a possible influence on the internal nanoparticle morphology, and the spectra are plotted in Fig. 1d. When excited in the polymer region ($\lambda_{ex} = 624$ nm), the FO*x*-T fluorescence was fully quenched, suggesting an intimate internal morphology, which favours the exciton dissociation generated in the polymer. However, one can clearly still see that the fluorescence of Y6 (800–1150 nm) is not totally quenched. Similar fluorescence results were observed with the PTQ10 : Y6 np-BHJ.[18] Concerning the influence of the side chain length, one can see a slightly higher quenching of the Y6 signal in the FO4-T : Y6 np-BHJ compared to FO6-T : Y6 and FO8-T : Y6 np-BHJ, 10% and 13%, respectively, relative to FO4-T : Y6. Except for this small difference, no significant influence of the polymer alkyl chain extension was observed, indicating that the aggregation behavior and crystallinity of the np-BHJ are largely preserved despite this structural modification. However, it should be noted that the internal FO*x*-T : Y6 nanoparticle morphology is not fully resolved, as cryo-TEM and PL quenching do not allow unambiguous determination of internal segregation or phase purity.

2.2 Water-processed OSC performances

The effect of the donor alkyl chain length on the processing of np-BHJ films was examined through the fabrication and characterization of organic solar cells (OSCs). The devices were fabricated using an inverted architecture: glass/ITO/ZnO/np-BHJ/MoO_3/Ag (see Fig. 2a). After deposition of the ZnO electron transport layer (ETL) onto the transparent ITO electrode, the various aqueous colloidal dispersions were spin-coated onto the UV-O_3-treated ETL surface. Subsequently, the np-BHJ films were subjected to thermal annealing at various temperatures ranging from 140 °C to 200 °C in an N_2 environment. Note that some layers were only dried at room temperature (RT) in the same

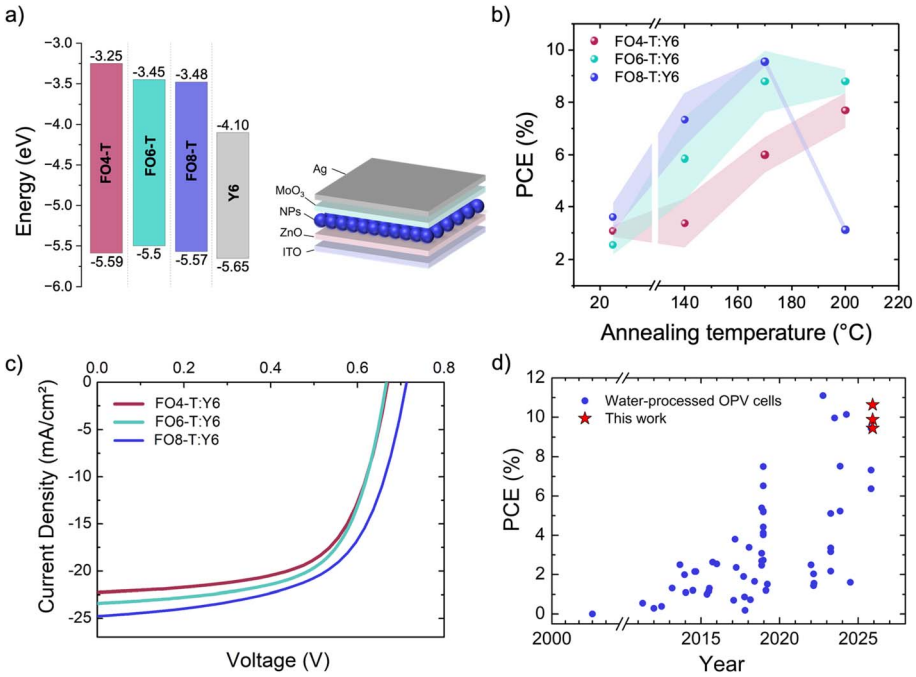

Fig. 2 (a) The energy levels[30] of the polymers and the NFA Y6 as well as the OSC device architecture used in this work. (b) Average PCE *vs.* the annealing temperature for the OSCs based on the active layers FO4-T : Y6, FO6-T : Y6 and FO8-T : Y6. Thick color bands correspond to the calculated standard deviation on 4 to 8 devices. (c) *J*–*V* curves from the FO*x*-T : Y6 hero cells corresponding to Table S3. (d) Efficiency evolution over the years of organic solar cells processed from water.

inert environment. The fabrication of OSCs was completed by thermally evaporating MoO_3 and Ag as the hole transport layer (HTL) and top electrode, respectively. Current density–voltage (*J*–*V*) characteristics of the three donor : acceptor systems with varying thermal annealing temperatures are presented in Table 1 and Fig. S5, and the power conversion efficiency (PCE) is summarized in Fig. 2b. Without any thermal treatment, the OSCs suffer from low efficiencies for all three systems, mainly due to modest short-circuit current density (J_{sc}). We assign this to the structure of the as-cast nanoparticulate film, where numerous grain boundaries at the NP interfaces can hinder the transport of photogenerated charges through the film.[34] When annealed at 140 °C, the FO8-T : Y6 NP-based OSC exhibits a strong improvement in both J_{sc} (19.99 mA cm^{-2}) and fill factor (FF, 0.56), leading to an average PCE of 7.33%. The two systems with shorter polymer sidechains also experienced similar a increase in J_{sc} but remained limited by their FF and open-circuit voltage (V_{oc}), with an average PCE of 5.85% and 3.38%

Table 1 Average OPV performances of optimised FO*x*-T : Y6 (1 : 1.2) np-BHJ and BHJ devices extracted from a minimum of 8 devices with varying annealing temperature

Active layer	Annealing temperature (°C)	J_{sc} (mA cm^{-2})	V_{oc} (V)	FF	PCE (%)
FO4-T : Y6 (1 : 1.2) np-BHJ	RT	11.16	0.62	0.44	3.08 ± 0.21
	140	19.25	0.45	0.38	3.38 ± 0.92
	170	22.01	0.58	0.47	6.00 ± 0.67
	200	20.66	0.62	0.60	7.69 ± 0.65
FO4-T : Y6 (1 : 1.2) BHJ[a]	100	22.72	0.75	0.58	9.80
FO6-T : Y6 (1 : 1.2) np-BHJ	RT	10.63	0.64	0.37	2.54 ± 0.37
	140	19.02	0.62	0.48	5.85 ± 1.59
	170	23.04	0.66	0.57	8.79 ± 1.16
	200	22.75	0.66	0.58	8.80 ± 0.45
FO6-T : Y6 (1 : 1.2) BHJ[a]	100	26.70	0.79	0.67	14.10
FO8-T : Y6 (1 : 1.2) np-BHJ	RT	12.45	0.68	0.42	3.61 ± 0.56
	140	18.99	0.69	0.56	7.33 ± 1.02
	170	21.47	0.69	0.65	9.54 ± 0.19
	200	11.81	0.48	0.55	3.12 ± 0.17
FO8-T : Y6 (1 : 1.2) BHJ[a]	100	24.16	0.79	0.57	10.7

[a] BHJ devices made with chloroform + DIO reported in a previous study.[30]

for FO6-T : Y6 and FO4-T : Y6, respectively. Increasing the annealing temperature to 170 °C further improved the performance of FO8-T : Y6, affording an average PCE of 9.54%, with a V_{oc} of 0.69 V, a J_{sc} of 21.47 mA cm^{-2}, and a FF of 0.65. Both FO6-T : Y6 and FO4-T : Y6 also benefited from annealing at this temperature, in particular the FO6-T : Y6 system, which reached an average PCE of 8.79%. At 200 °C, the blends with shorter side chains (FO4-T : Y6 and FO6-T : Y6) achieved their optimal performances with an average PCE of 7.69% and 8.80%, respectively. As typically observed in NP-based OSCs, the FF was the parameter that was the most enhanced at elevated annealing temperatures. Surprisingly, FO8-T : Y6 deviated from this trend, with a large drop in all PV parameters (V_{oc}, J_{sc} and FF), leading to a decrease in PCE to an average of 3.12%. These results reveal three distinct trends among the systems. The FO8-T : Y6 np-BHJ OSC exhibits an optimal annealing temperature of 170 °C, followed by a sharp decline at higher temperatures. The FO6-T : Y6 np-BHJ OSC also reaches its optimal efficiency at 170 °C, followed by a plateau in performance when annealed at higher temperatures. In contrast, the FO4-T : Y6 np-BHJ OSC requires higher temperatures to reach the same performance as the OSCs based on longer alkyl chains, with an optimal temperature of 200 °C.

The changes in optical absorption of the np-BHJ films were also investigated with UV-visible spectra as well as the external quantum efficiency (EQE) spectra of the corresponding devices. The absorbance of the np-BHJ films dried and annealed at 140 °C, 170 °C and 200 °C is shown in Fig. S6. For each condition, the ratio between the Y6 peak (around 840 nm) and the FO*x*-T polymer peak (around 675 nm) was calculated. This ratio increases with the side chain length and at all annealing temperatures. These results suggest that when subjected to thermal energy, the organization inside the composite particles tends to be more affected with increasing the polymer's side chain length. Furthermore, the drop in performance observed for the FO8-T : Y6 np-BHJ OSCs annealed at 200 °C is explained by the EQE, which shows a major decrease in photogenerated charges, likely due to increasing geminate recombination (see Fig. S7). Again, such a change indicates a strong influence of the side-chain length on the processing and hence the thin film morphology prepared from nanoparticles, which will be discussed in the next section.

The np-BHJ OSC performances have been compared with those of OSC devices processed using chloroform and DIO solutions (noted as BHJ) obtained in a previous study.[30] The BHJ OSCs (FO*x*-T : Y6, ratio 1 : 1.2) do not show the same trend in performance as the water-processed devices (Table 1). When processed from organic solvents, the FO6-T : Y6 BHJ devices clearly show higher efficiencies than both FO4-T : Y6 and FO8-T : Y6 BHJ devices.[30] In this regard, a larger performance gap is observed between FO6-T : Y6 np-BHJ solar cells and their organic solvent-processed counterpart FO6-T : Y6 BHJ, with a PCE of 8.80% and 14.10%, respectively. By contrast, the FO8-T : Y6 np-BHJ show only a small difference from their BHJ equivalents, with a PCE of 9.54% and 10.70% achieved respectively. Lastly, FO4-T : Y6 np-BHJ also show lower performance compared to FO4-T : Y6 BHJ, with a PCE of 7.69% and 9.8% PCE, respectively. These differences in all np-BHJ FO*x*-T : Y6 OSC devices are mostly due to a lower J_{sc} compared to that of BHJ FO*x*-T : Y6 devices. This difference can be explained by the residual Y6 fluorescence observed in np-BHJ, suggesting that not all excitons formed in Y6 are dissociated, thereby increasing geminate recombination. In addition, the V_{oc} of np-BHJ OSC is slightly lower in all cases than that of BHJ OSC by ~100 mV and a similar kind of difference was also observed for PTQ10 : Y6.[18] The origin of such loss is still unclear, and work is currently ongoing to understand its cause (lower CT state energy, increased recombinations, *etc.*).

Nevertheless, when optimized with the proper thickness (around 170 nm), annealing time (2 min), and filtration, the FO8-T : Y6 np-BHJ devices reached a record efficiency of 10.64% (and average 10.40%), hence closing the gap with the BHJ devices (see Table S3). The J_{sc} achieved for FO8-T : Y6 np-BHJ is similar to that of its BHJ counterpart (24.17 and 24.16 mA cm^{-2}, respectively). Although a V_{oc} loss of 83 mV is noted, this is balanced by the larger FF (0.61 *versus* 0.57), allowing the water-processed devices to compete with their organic solvent-processed counterparts. Notably, this PCE ranks among the best performances reported for water-processed OSCs, in particular those utilizing nanoparticles produced by mini-emulsion methods (Fig. 2d). In addition, higher performances were also obtained with FO4-T : Y6 and FO6-T : Y6 np-BHJ OSCs thanks to slight optimisation of the thicknesses (around 180 nm) and process (filtration), and PCEs up to 9.45% (average 9.01%) and 9.88% (average 9.05%), respectively, were achieved (Table S3). These results demonstrate a good compatibility of the FO*x*-T polymer library with this environmentally friendly process.

2.3 Correlation between the film microstructure and OSC performances

Differential scanning calorimetry (DSC) was conducted to probe the thermal transitions of the polymers and Y6 (thermograms are provided in Fig. S8–10). Two sets of samples were investigated: FO*x*-T : Y6 blends cast from chloroform solutions and the corresponding nanoparticles. In the chloroform-cast blends, the glass transition temperatures (T_g) of Y6, FO6-T, and FO8-T were observed at 210 °C, 180 °C, and 120 °C, respectively, whereas FO4-T displayed no detectable T_g. Thus, the increase in the side-chain length leads to a progressive decrease in the glass transition temperatures of the polymers, consistent with enhanced chain flexibility and resulting in the highest bulk segregation for the FO8-T : Y6 blend, leading to the decrease in OPV performance for the devices annealed at 200 °C. For all three blends polymer : Y6, a cold crystallization event was recorded between 220 and 230 °C, attributed to Y6, occurring once its T_g was exceeded and molecular rearrangement became possible. In a blend with FO4-T, bearing the shortest alkyl side chains, Y6 exhibits a single melting transition at 290 °C, consistent with crystallization behavior analogous to the neat acceptor and indicative of limited intermolecular interactions. Incorporation of FO6-T, with intermediate side chain lengths, results in two distinct melting transitions at 290 °C and 310 °C,

evidencing the coexistence of neat-like Y6 domains and a stabilized crystalline polymorph promoted by the polymer environment. By contrast, blending with FO8-T, which possesses the longest alkyl substituents, yields exclusively the higher-temperature transition at 310 °C, demonstrating strong side-chain-mediated interactions that favor the formation of a distinct and thermally robust Y6 crystalline phase. Several Y6 melting peaks were also reported by Zhou *et al.* in the case of the PM6 : Y6 blend cast from different solvents, and these were also linked to the donor–acceptor thin film morphology driven by the solvent.[35]

DSC characterization of the nanoparticles was limited to 240 °C to prevent SDS degradation within the instrument (Fig. S9). The analysis consistently revealed an additional transition at 95 °C, attributed to SDS melting. Cold crystallization of Y6 was observed in both pure Y6 nanoparticles and all polymer : Y6 blends around 225 °C, indicating that the miniemulsion process partially restricts its crystallization. A melting signal at 195 °C was detected in pure Y6 and FO4-T : Y6 nanoparticles, similar to observations previously reported for PTQ10 : Y6 nanoparticles prepared *via* miniemulsion.[19] This feature is unlikely to arise solely from SDS, as it was not observed in all samples, nor from Y6 melting, which occurs near 300 °C. While further experiments are required to confirm its origin, the signal may result from co-crystallization between SDS and Y6 at the nanoparticle surface.

To clarify the trends observed with varying alkyl chain length and thermal annealing, the np-BHJ films were characterized using atomic force microscopy (AFM) and grazing incidence wide-angle X-ray scattering (GIWAXS) and the results are presented in Fig. 3 and in S11–S15. All the samples were prepared under the same conditions as the OPV devices. In the 2D GIWAXS pattern of the FO8-T : Y6 NPs without annealing, we observe a thin film morphology with no preferential orientation, indicated by the presence of isotropic scattering halos. At low q values, the main reflection observed is assigned to the FO8-T (100) lamellae ($q_{100} = 2.7$ nm^{-1}),[30] while the reflection at $q = 17.9$ nm^{-1} corresponds to a combination of the FO8-T (010) planes and the π–π stacking of Y6,[36] here assigned by direct comparison with films annealed at higher temperatures (see Fig. 3a and b). This agrees with what we previously observed for this polymer : acceptor blend in BHJ (non-NP) films.[30] In pristine FO8-T and Y6 films, the (010) and π–π stacking reflections appear too close in q-space, so that they cannot be unambiguously ascribed to either the donor or acceptor material in this work. Here, the reflection appearing at high q values (typically 17.6–18.0 nm^{-1}) is fitted using a single pseudo-Voigt peak. However, upon annealing at 140 °C, *i.e.* just above the T_g of FO8-T, distinct scattering features arise in the oop direction correlating to Y6 that coexist with the FO8-T lamellae. In addition, one can observe that thermal annealing induces a favorable orientation of the π–π stacking in the out-of-plane (oop) direction, with a stronger diffraction peak appearing, thus signaling a transition from isotropic (at RT) to oriented films. At 170 °C, this effect is even more pronounced, with stronger scattering intensity values for the periodic aromatic–aliphatic packing of Y6 in the oop direction.[37] For this blend, upon annealing at 200 °C, the Y6 diffraction features partly fade out while those of FO8-T are enhanced, which eventually leads to a disruption in the microstructure. Since this temperature is well above the T_g of FO8-T ($T_g = 120$ °C) and approaches the T_g of Y6 ($T_g = 210$ °C), polymer and NFA molecules can both be mobile and segregate. Cold crystallization of Y6 can also happen, with both phenomena explaining the morphological changes. When interpreting the AFM images, we focus on the smaller scale images (0.5 μm × 0.5 μm), but the root-mean-square (RMS) roughness was determined from larger scale images (2 μm × 2 μm). The AFM images correlate well with these findings (see Fig. 3c), with RMS surface roughness decreasing from 8.4 nm to 6.3 nm with increasing TA temperature (RT to 170 °C; see Fig. S11), but at 200 °C the roughness is larger again ($R_{rms} = 35$ nm), due to the crystallization and thus stronger aggregation of Y6. This phenomenon is likely the result of enhanced molecular mobility for an annealing temperature exceeding T_g of FO8-T ($T_g = 120$ °C) and approaching that of Y6 ($T_g = 210$ °C).

Reduction of the side chain from FO8 to FO6 (and FO4) leads to a decrease in the lamellar stacking distance, as evidenced by the shift of the (100) peak toward higher q values (see Table S4). NP films of FO6-T and Y6 exhibited comparable features in the 2D GIWAXS patterns (see Fig. S12). In the pristine (non-annealed) films, only the (100) and π–π scattering peaks were detected, with no clear preferential orientation. Upon annealing at 140 °C, distinct oop peaks appeared, evidencing the development of more ordered Y6 domains. This effect is slightly more pronounced after annealing at 170 °C, while at 200 °C the sharp oop reflections mostly disappear and the (100) peak of FO6-T dominates. A preferential orientation of the π–π stacking is also observed with a stronger diffraction peak in the oop direction for 170 and 200 °C TA films. Interestingly, the Y6 morphology in the nanoparticle-based thin films seems to be more stabilized in blends with FO6-T, as compared to FO8-T, since we do not observe reduction in polymer ordering. However, the AFM images (Fig. S13) seem to indicate surface melting upon annealing at 200 °C. In contrast, FO4-T : Y6 blends are comparatively less crystalline and more isotropic, as indicated by the oop lamellar 100 and π–π peaks appearing with reduced intensity (Fig. S14). Higher annealing temperatures increase the order slightly, especially after annealing at 170 °C, and only after annealing at 200 °C do the features appear more distinct including the appearance of an isotropic halo attributed to the disordered side-chains of FO4-T. Overall, in FO4-T : Y6 the preferential orientation of the π–π stacking upon annealing is not as clear as that observed for FO6-T : Y6 and FO8-T : Y6 NPs. One can suggest that, since FO4-T has an ill-defined or very high T_g, the polymer backbones and Y6 molecules do not have the mobility to reorganize as much as in the other systems. In addition, for FO4-T, the degree of disorder appears to be substantially higher; consequently, a more ordered state is observed only when Y6 begins to form crystallites.

Overall, the oop orientation appeared to be favored upon thermal annealing for all three polymers, although it is more pronounced for FO6-T : Y6 and FO8-T : Y6 NP layers. The AFM

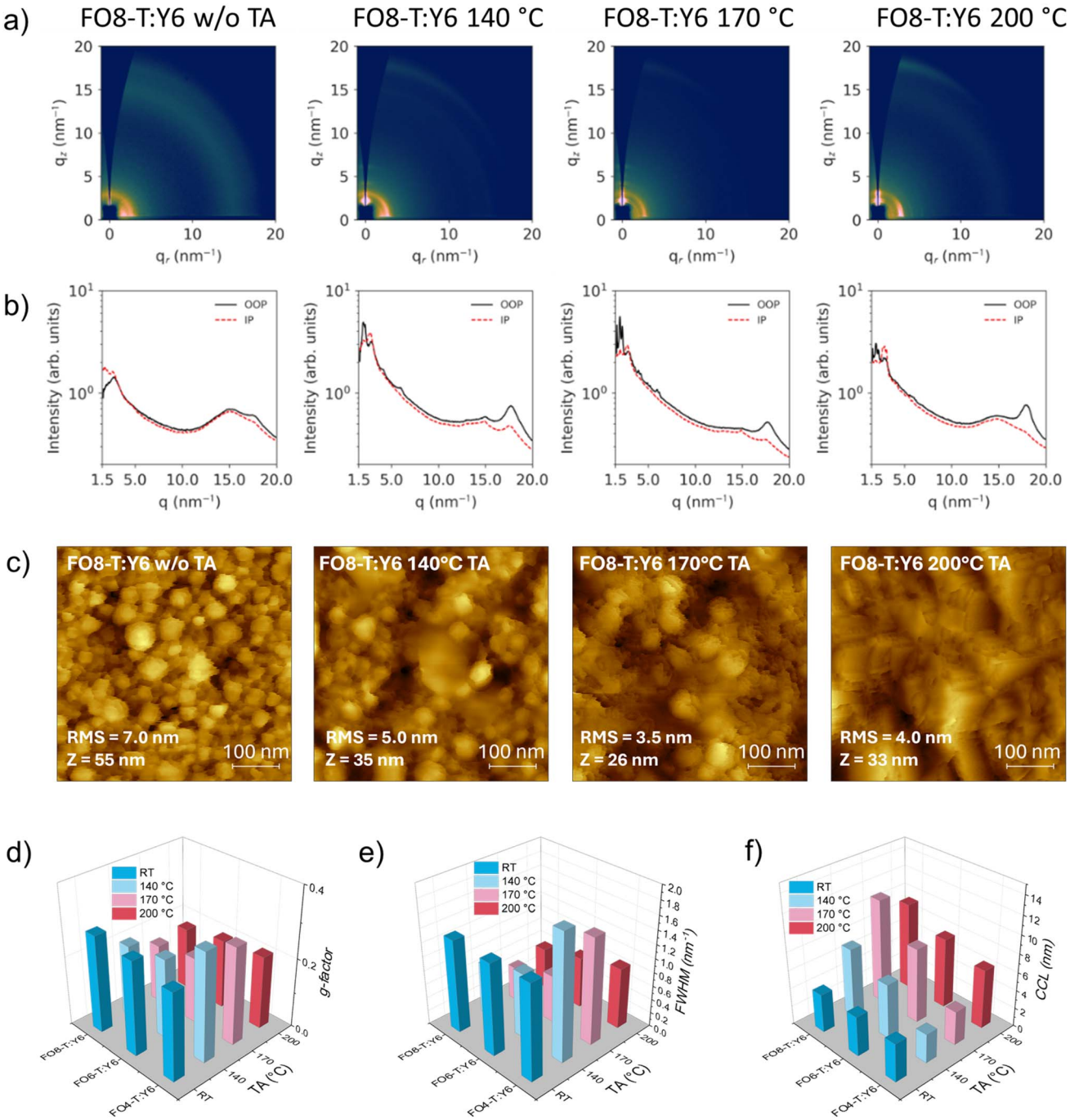

Fig. 3 Morphological characterization of NP films. (a) 2D GIWAXS patterns and (b) 1D line plots of FO8-T : Y6 (1 : 1.2) annealed at different temperatures. (c) AFM images of FO8-T : Y6 blends annealed at different temperatures. (d) *g*-Factor, (e) FWHM and (f) CCL extracted from the (100) polymer planes obtained by GIWAXS for the different blends with Y6 annealed at different temperatures.

images for FO4-T : Y6 NP layers (Fig. S15 and S11) show a significant decrease in roughness (R_{rms}) from 9.2 nm (w/o TA) to 8.9 nm upon annealing at 170 °C, and at 200 °C the coalescence of the NPs can be observed (R_{rms} = 3.4 nm). The key figures of the GIWAXS analysis are presented in Fig. 3d–f and Tables S4 and S5 for the three different polymer blends annealed at different temperatures. Assuming that the peak width is governed by the crystallite size, the crystallite size can be inferred from the full width at half maximum (FWHM) of the diffraction peaks (Fig. 3e) and the corresponding X-ray coherence length (CCL, Fig. 3f). For the (100) planes attributed to the polymer lamellae, the FWHM decreases with increasing annealing temperature for the FO8-T and FO6-T blends, indicating improved ordering, but it broadens again at 200 °C. This behavior is attributed to the formation of Y6 crystallites at temperatures approaching the glass transition temperature of

Y6, which not only affects the packing of the polymer (100) planes but also is consistent with the cold crystallization observed in DSC. The minimum FWHM, corresponding to the most ordered domains, differs among the polymers: for FO6-T and FO8-T the optimum occurs at 170 °C, whereas for FO4-T it appears at 200 °C. This suggests that FO4-T exhibits a generally higher initial degree of disorder, with improved ordering happening only when the annealing temperature is close to the T_g of Y6, thereby giving more mobility to Y6 which begins to crystallize. FO6-T and FO8-T display broadly similar trends, although FO8-T shows smaller FWHM values (greater order) at 170 °C.

For the π–π reflections, the FWHM decreases with increasing annealing temperature, but remains broader overall compared to the lamellar peaks (see SI). The g value corresponds to the paracrystalline disorder parameter, which quantifies the extent of structural disorder within the crystalline regions of a polymer and is defined as follows:

$$g = \sqrt{\frac{\mathrm{FWHM}}{2\pi q}}$$

A g value of 0 denotes a perfectly ordered crystal with no lattice distortion, while increasing g values reflect greater paracrystalline disorder, *i.e.*, enhanced randomness or irregularity in lattice spacing.[38] Here, the g values exhibit trends similar to the FWHM of the (100) plane (see Fig. 3d). However, for the π–π planes, the difference between 170 °C and 200 °C is negligible, with little to no variation observed across the polymers (see SI). Similarly, the X-ray coherence length (CCL, defined as $2\pi K/\mathrm{FWHM}$, with $K = 0.9$) provides insight into crystalline domain size and order, with larger CCL values reflecting higher quality crystallinity, which often correlates with enhanced electronic and optical properties in organic polymer films.[39] For the (100) plane, the CCL increases sharply with annealing temperature up to 170 °C for all three polymers, after which the behaviour diverges. FO4-T exhibits relatively small CCL values overall, with a maximum of 6.5 nm at 200 °C. In FO6-T, the maximum CCL of 8.1 nm occurs at 170 °C, with only a slight reduction at 200 °C. FO8-T shows the highest overall CCL values, reaching maximum of 11.3 nm and 9.5 nm after annealing at 170 °C and 200 °C, respectively. For the π–π reflections, the CCL increases with annealing temperature for all three polymers, although the effect is minimal for FO4-T : Y6, suggesting that thermal annealing has little influence on π–π stacking coherence in such a blend. In contrast, FO6-T and FO8-T exhibit a pronounced response, with the CCL approximately doubling upon annealing and reaching maximum values at 200 °C.

The microstructural changes can be correlated with the device performance. It is, indeed, possible to attribute the higher performance of FO8-T : Y6 devices annealed at 170 °C to the increase in the FF, most likely due to a more favorable microstructure in the NPs and in the thin film upon sintering. The drop in the PCE at higher thermal annealing can be correlated with, on the one hand, the formation of the large Y6 domains apparent in the AFM images leading to the drop in J_{sc} and, on the other hand, with the reduced order in the microstructure and hence a significant drop in the FF. For the FO6-T : Y6 np-BHJ thin film, thermal annealing is also necessary to create interconnection between the nanoparticles and improve the ordering of the polymer chains and π–π stacking, thereby improving the PV performances. However, the PCEs of FO6-T : Y6 devices annealed at 170 °C and 200 °C do not show any differences, in accordance with the almost unchanged microstructure detected by GIWAXS. For the FO4-T : Y6 np-BHJ thin film, thermal treatment was also shown to be necessary to improve the connection of the nanoparticles and enhance polymer and molecular ordering. Notably, the best performance in OPV devices was obtained for the FO4-T : Y6 blend after thermal annealing at 200 °C, which again coincides with the most ordered thin film morphology according to GIWAXS analysis. These findings suggest that alkyl side-chain length modulates polymer chain mobility during thermal annealing, with longer chains (FO8-T) enabling earlier formation of ordered lamellar and π–π stacking due to their low T_g (120 °C), while shorter chains (FO4-T), having no or ill-defined T_g, require higher temperatures. Consequently, a structural evolution model emerges in which side-chain-mediated mobility controls Y6 and polymer crystallization, governing nanoparticle sintering and ultimately device performance.

3 Conclusion

In summary, we investigated how altering alkyl side-chain lengths in FO4-T, FO6-T and FO8-T polymers impacts the internal nanoparticle morphology as well as that of nanoparticle-based thin films and their resulting photovoltaic performances. While no significant influence of this structural modification was observed on the nanoparticle internal morphology among all three FO*x*-T : Y6 systems, contrasted features upon thermal annealing were revealed and correlated with the OPV results. It was found that extending the polymer sidechains could benefit the nanoparticles to form a more ordered and crystalline film. In thin films, the FO4-T based particles (shortest chains) required high-temperature annealing for inter-particle coalescence and to impose an ordered microstructure, while FO8-T based nanoparticles self-organized favorably at lower temperatures. As a result, OPV devices prepared with the FO8-T : Y6 blend already reach high performance at 140 °C, with an optimal treatment at 170 °C, resulting in a record 10.64% PCE (miniemulsion prepared NP OPVs). These findings reveal that nanoparticle-based thin films made with long-sidechain polymers exhibit enhanced microstructural arrangement during thermal annealing. This approach presents a promising design strategy to lower processing temperatures for water-processed OSCs, overcoming the high-temperature sintering requirements typically associated with highly crystalline mini-emulsion nanoparticles.

4 Experimental section

Experimental details and polymer and nanoparticle characterization are described in the SI.

Author contributions

H. L.: conceptualisation, formal analysis, investigation, methodology, writing – original draft; M. R.: conceptualisation, formal analysis, investigation, methodology, writing – original draft; A. P.-V.: investigation, formal analysis, writing – review & editing; X. R.-M.: investigation, formal analysis, writing – review & editing; G. P.: investigation, writing – review & editing; M. S.: investigation, writing – review & editing; A. S.-V.: investigation; C. L.-D.: formal analysis, writing – review & editing; A. B.: investigation, formal analysis, writing – review & editing; G. W.: supervision, writing – review & editing; J. M.: formal analysis, validation, funding acquisition, writing – review & editing; M. H.: formal analysis, validation, funding acquisition, writing – review & editing; S. C.: conceptualisation, formal analysis, investigation, methodology, funding acquisition, supervision, writing – original draft.

Conflicts of interest

The authors declare no conflicts of interest.

Data availability

The data supporting this article have been included in the manuscript and as part of the supplementary information (SI). Supplementary information includes: methods; polymer characterisation: Table S1 and Fig. S1; nanoparticle characterisation: Fig. S2–S4 and Table S2; device characterisation: Fig. S5–S7 and Table S3; thermal characterisation: Fig. S8–S10; morphological characterisation: Fig. S11–S15 and Tables S4 and S5. See DOI: https://doi.org/10.1039/d6ta00092d.

Acknowledgements

M. R. and M. H. thank the Engineering and Physics Science Research Council (EPSRC) (EP/R513052/1). H. L., G. W. and S. C. acknowledge the support provided by the ANR through the WATER-PV project No. ANR-20-CE05-0002. GIWAXS experiments were performed at the NCD-SWEET beamline at ALBA Synchrotron (experiment ID AV-2024098865) with the collaboration of ALBA staff. A. P. V., X. R.-M. and J. M. acknowledge the European Research Council (Grant 101086805).

References

1 C. Li, Y. Cai, P. Hu, T. Liu, L. Zhu, R. Zeng, F. Han, M. Zhang, M. Zhang, J. Lv, Y. Ma, D. Han, M. Zhang, Q. Lin, J. Xu, N. Yu, J. Qiao, J. Wang, X. Zhang, J. Xia, Z. Tang, L. Ye, X. Li, Z. Xu, X. Hao, Q. Peng, F. Liu, L. Guo and H. Huang, *Nat. Mater.*, 2025, **24**, 1626–1634.

2 J. Zhu, R. Zeng, E. Zhou, C. Li, J. Deng, M. Du, Q. Guo, M. Ji, Z. Wang, Y. Lin, F. Han, J. Zhuang, S. Tan, L. Kan, L. Zhu, M. Zhang and F. Liu, *J. Am. Chem. Soc.*, 2025, **147**, 24491–24501.

3 M. Du, N. Sun, H. Cheng, X. Liu, X. Yi, Q. Guo, Q. Guo, M. Lv, J. Yao, L. Hu, Z. Li, Z. Zheng, C. Shan, A. K. K. Kyaw, G. Li, Q. Xia, H. Zuilhof and E. Zhou, *Angew. Chem., Int. Ed.*, 2025, **64**, e202515114.

4 I. McCulloch, M. Chabinyc, C. Brabec, C. B. Nielsen and S. E. Watkins, *Nat. Mater.*, 2023, **22**, 1304–1310.

5 E. Mazzolini, R. A. Pacalaj, Y. Fu, B. R. Patil, R. Patidar, X. Lu, T. M. Watson, J. R. Durrant, Z. Li and N. Gasparini, *Adv. Sci.*, 2024, **11**, 2402637.

6 B. Liu, O. J. Sandberg, J. Qin, Y. Liu, S. Wilken, N. Wu, X. Yu, J. Fang, Z. Li, R. Huang, W. Zha, Q. Luo, H. Tan, R. Österbacka and C.-Q. Ma, *Nat. Photonics*, 2025, **19**, 195–203.

7 N. Yang, S. Zhang, Y. Cui, J. Wang, S. Cheng and J. Hou, *Nat. Rev. Mater.*, 2025, **10**, 404–424.

8 R. Sun, X. Yuan, X. Yang, Y. Wu, Y. Shao, X. Wu, C. J. Brabec and J. Min, *Joule*, 2024, **8**, 2523–2538.

9 P. Xue, P. Cheng, R. P. S. Han and X. Zhan, *Mater. Horiz.*, 2022, **9**, 194–219.

10 S. Pang, Z. Chen, J. Li, Y. Chen, Z. Liu, H. Wu, C. Duan, F. Huang and Y. Cao, *Mater. Horiz.*, 2023, **10**, 473–482.

11 R. Zeng, F. Han, W. Zhong, M. Zhang, S. Tan, Y. Lin, J. Deng, G. Zhou, L. Kan, L. Zhu, X. Gao, J. Zhu, W. Zhao, S. Xu, X. Xue, B. Hao, Z. Zhou, X. Wu, C. Wang, Z. Fink, Z. Tang, H. Jing, T. P. Russell, Y. Zhang and F. Liu, *Adv. Mater.*, 2025, **37**, 2501812.

12 D. Corzo, D. Rosas-Villalva, A. C, G. Tostado-Blázquez, E. B. Alexandre, L. H. Hernandez, J. Han, H. Xu, M. Babics, S. De Wolf and D. Baran, *Nat. Energy*, 2023, **8**, 62–73.

13 J. Panidi, E. Mazzolini, F. Eisner, Y. Fu, F. Furlan, Z. Qiao, M. Rimmele, Z. Li, X. Lu, J. Nelson, J. R. Durrant, M. Heeney and N. Gasparini, *ACS Energy Lett.*, 2023, **8**, 3038–3047.

14 C. M. Alder, J. D. Hayler, R. K. Henderson, A. M. Redman, L. Shukla, L. E. Shuster and H. F. Sneddon, *Green Chem.*, 2016, **18**, 3879–3890.

15 T. Kietzke, D. Neher, K. Landfester, R. Montenegro, R. Güntner and U. Scherf, *Nat. Mater.*, 2003, **2**, 408–412.

16 A. Holmes, E. Deniau, C. Lartigau-Dagron, A. Bousquet, S. Chambon and N. P. Holmes, *ACS Nano*, 2021, **15**, 3927–3959.

17 C. Xie, T. Heumüller, W. Gruber, X. Tang, A. Classen, I. Schuldes, M. Bidwell, A. Späth, R. H. Fink, T. Unruh, I. McCulloch, N. Li and C. J. Brabec, *Nat. Commun.*, 2018, **9**, 5335.

18 H. Laval, A. Holmes, M. A. Marcus, B. Watts, G. Bonfante, M. Schmutz, E. Deniau, R. Szymanski, C. Lartigau-Dagron, X. Xu, J. M. Cairney, K. Hirakawa, F. Awai, T. Kubo, G. Wantz, A. Bousquet, N. P. Holmes and S. Chambon, *Adv. Energy Mater.*, 2023, **13**, 2300249.

19 A. Holmes, H. Laval, M. Guizzardi, V. Maruzzo, G. Folpini, N. Barbero, E. Deniau, M. Schmutz, S. Blanc, A. Petrozza, G. M. Paternò, G. Wantz, S. Chambon, C. Lartigau-Dagron and A. Bousquet, *Energy Environ. Sci.*, 2024, **17**, 1107–1116.

20 C. Xie, X. Zeng, C. Li, X. Sun, S. Liang, H. Huang, B. Deng, X. Wen, G. Zhang, P. You, C. Yang, Y. Han, S. Li, G. Lu, H. Hu, N. Li and Y. Chen, *Energy Environ. Sci.*, 2024, **17**, 2441–2452.

21 S. Lee, D. Jeong, C. Kim, C. Lee, H. Kang, H. Y. Woo and B. J. Kim, *ACS Nano*, 2020, **14**, 14493–14527.

22 C. Duan, R. E. M. Willems, J. J. van Franeker, B. J. Bruijnaers, M. M. Wienk and R. A. J. Janssen, *J. Mater. Chem. A*, 2016, **4**, 1855–1866.
23 D. Yuan, G. Qin, L. Zhang, F. Pan, R. Qiu, S. Lei, S. Deng and J. Chen, *ACS Appl. Mater. Interfaces*, 2021, **13**, 57654–57663.
24 J. Mei and Z. Bao, *Chem. Mater.*, 2014, **26**, 604–615.
25 Z. Li, R. Ding, X. Gu, C. e. Zhang, J. Lv, Y. Han, J. Chen, Y. Cai, X. Zhang and H. Huang, *Chem. Commun.*, 2025, **61**, 8659–8662.
26 M. Li, P. J. Leenaers, M. M. Wienk and R. A. J. Janssen, *J. Mater. Chem. C*, 2020, **8**, 5856–5867.
27 K. N. Schwarz, S. B. Farley, T. A. Smith and K. P. Ghiggino, *Nanoscale*, 2015, **7**, 19899–19904.
28 H. Laval, Y. Tian, V. Lafranconi, M. Barr, P. Dastoor, M. M. Marcus, G. Wantz, N. P. Holmes, K. Hirakawa and S. Chambon, *Small*, 2024, **20**, 2404112.
29 M. G. Barr, S. Chambon, A. Fahy, T. W. Jones, M. A. Marcus, A. L. D. Kilcoyne, P. C. Dastoor, M. J. Griffith and N. P. Holmes, *Mater. Chem. Front.*, 2021, **5**, 2218–2233.
30 M. Rimmele, Z. Qiao, J. Panidi, F. Furlan, C. Lee, W. L. Tan, C. R. McNeill, Y. Kim, N. Gasparini and M. Heeney, *Mater. Horiz.*, 2023, **10**, 4202–4212.
31 E. Mazzolini, Z. Qiao, J. Muller, F. Furlan, M. Sanviti, D. Nodari, M. Rimmele, A. Collauto, C. Deibel, M. Heeney, J. Martin, F. Eisner, J. Nelson, N. Gasparini and J. Panidi, *Adv. Energy Mater.*, 2025, 2405635.
32 J. Yuan, Y. Zhang, L. Zhou, G. Zhang, H.-L. Yip, T.-K. Lau, X. Lu, C. Zhu, H. Peng, P. A. Johnson, M. Leclerc, Y. Cao, J. Ulanski, Y. Li and Y. Zou, *Joule*, 2019, **3**, 1140–1151.
33 W. Yue, Y. Zhao, S. Shao, H. Tian, Z. Xie, Y. Geng and F. Wang, *J. Mater. Chem.*, 2009, **19**, 2199–2206.
34 C. Xie, A. Classen, A. Späth, X. Tang, J. Min, M. Meyer, C. Zhang, N. Li, A. Osvet, R. H. Fink and C. J. Brabec, *Adv. Energy Mater.*, 2018, **8**, 1702857.
35 G. Yao, Y. Ge, X. Xiao, L. Zhang, N. Yi, H. Luo, S. Yuan and W. Zhou, *ACS Appl. Energy Mater.*, 2022, **5**, 1193–1204.
36 E. Gutierrez-Fernandez, A. D. Scaccabarozzi, A. Basu, E. Solano, T. D. Anthopoulos and J. Martín, *Adv. Sci.*, 2022, **9**, 2104977.
37 S. Marina, A. D. Scaccabarozzi, E. Gutierrez-Fernandez, E. Solano, A. Khirbat, L. Ciammaruchi, A. Iturrospe, A. Balzer, L. Yu, E. Gabirondo, X. Monnier, H. Sardon, T. D. Anthopoulos, M. Caironi, M. Campoy-Quiles, C. Müller, D. Cangialosi, N. Stingelin and J. Martin, *Adv. Funct. Mater.*, 2021, **31**, 2103784.
38 S. Marina, E. Gutierrez-Fernandez, J. Gutierrez, M. Gobbi, N. Ramos, E. Solano, J. Rech, W. You, L. Hueso, A. Tercjak, H. Ade and J. Martin, *Mater. Horiz.*, 2022, **9**, 1196–1206.
39 X. Song, N. Gasparini, M. M. Nahid, H. Chen, S. M. Macphee, W. Zhang, V. Norman, C. Zhu, D. Bryant, H. Ade, I. McCulloch and D. Baran, *Adv. Funct. Mater.*, 2018, **28**, 1802895.